Optimally-Tailored Spinodal Architected Materials for Multiscale Design and Manufacturing

*Fernando V. Senhora, Emily D. Sanders, and Glaucio H. Paulino**

Spinodal architected materials with tunable anisotropy unify optimal design and manufacturing of multiscale structures. By locally varying the spinodal class, orientation, and porosity during topology optimization, a large portion of the anisotropic material space is exploited such that material is efficiently placed along principal stress trajectories at the microscale. Additionally, the bicontinuous, nonperiodic, unstructured, and stochastic nature of spinodal architected materials promotes mechanical and biological functions not explicitly considered during optimization (e.g., insensitivity to imperfections, fluid transport conduits). Furthermore, in contrast to laminated composites or periodic, structured architected materials (e.g., lattices), the functional representation of spinodal architected materials leads to multiscale, optimized designs with clear physical interpretation that can be manufactured directly, without special treatment at spinodal transitions. Physical models of the optimized, spinodal-embedded parts are manufactured using a scalable, voxel-based strategy to communicate with a masked stereolithography (m-SLA) 3D printer.

1. Introduction

The great diversity of microarchitectures in biological materials (see **Figure 1**) are both the result of formation processes and the need to support a multitude of mechanical and biological functions (e.g., enabling fluid transport, facilitating regrowth and repair, and resisting uncertain and temporally-varying mechanical demands).[1–3] The Wolf–Roux (mechanostat) law, which suggests that bone is deposited or resorbed in response to changes in mechanical demands,[1,4,5] states that optimization plays a role in natural design of multiscale materials and structures. Thus, structural optimization is an attractive strategy for pursuit of biomimetic engineered systems with optimized performance; however, the range of functionality observed in nature is exceedingly difficult to fully integrate into an optimization-based engineering design process. Here, we endow a structural optimization approach with spinodal architected materials that mimic several microstructural characteristics observed in nature such that we directly target stiffness and lightweightness in design and indirectly promote other mechanical and biological functions that are facilitated by spinodal porosity and randomness at the microscale.

Figure 1 shows microstructures observed in several biological systems with varying pore size, pore shape, density, and directional preference—features that can be readily imitated by spinodal architected materials. Spinodal architected materials are obtained by interpreting one phase in a spinodal phase decomposition as a microstructural-material. Their unstructured, stochastic, microstructural features have been shown to contribute to desirable engineering properties (e.g., high mechanical resilience,[9] high energy absorption,[10] and insensitivity to imperfections[11]) that often exceed those of structured architected materials (e.g., truss and plate lattices). Furthermore, a functional approximation of the spinodal phase decomposition, in the form of a Gaussian random field (GRF),[12,13] enables broad tunability of microscale anisotropy and porosity for significant microarchitecture design freedom.[6] The underlying functional representation also makes it trivial to transition between different spinodal classes (e.g., the isotropic, cubic, lamellar, and columnar architectures shown in Figure 1) with arbitrary orientation and porosity. Thus, spinodal architected materials provide an avenue toward engineered parts with embedded, spatially-varying microscale features that have increased engineering performance and enhanced manufacturability relative to structured architected materials.

The manufacturing versatility of spinodal architected materials also enables a return to the classical multiscale

F. V. Senhora
School of Civil and Environmental Engineering
Georgia Institute of Technology
790 Atlantic Drive NW, Atlanta, GA 30332, USA
E. D. Sanders
George W. Woodruff School of Mechanical Engineering
Georgia Institute of Technology
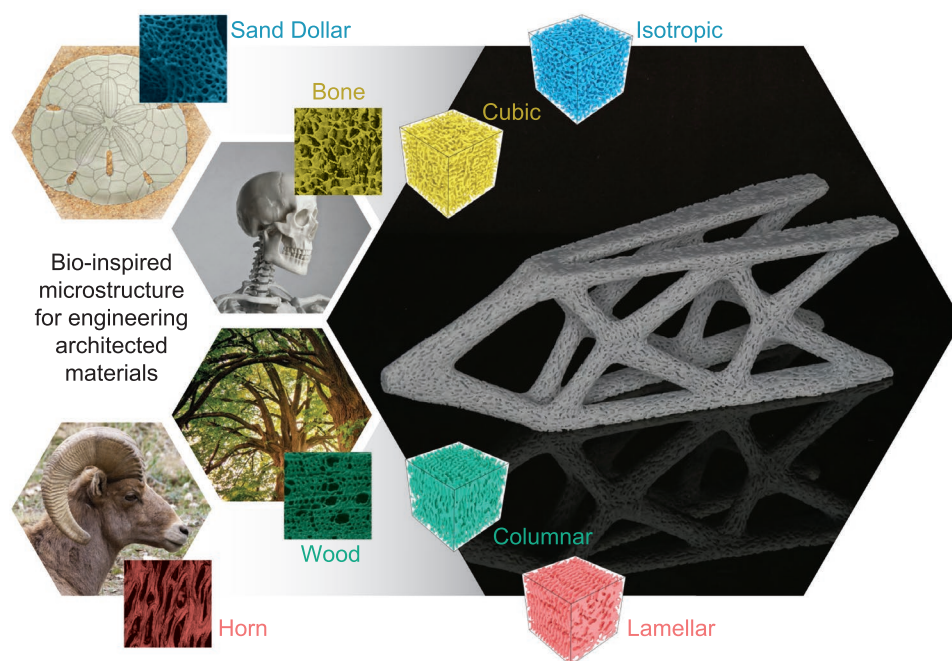Atlanta, GA 30332, USA
G. H. Paulino
Department of Civil and Environmental Engineering
Princeton University
Princeton, NJ 08544, USA
E-mail: gpaulino@princeton.edu
G. H. Paulino
Princeton Institute for the Science and Technology of Materials
Princeton University
Princeton, NJ 08544, USA

Figure 1. Spinodal architected materials with tunable anisotropy enable biomimicry of mechanical and biological function in engineered systems. Isotropic, cubic, lamellar, and columnar spinodal architected materials,[6] which bear similarities to, for example, the microstructures of a sand dollar, trabecular bone, wood, and the horn of a bighorn sheep, respectively, are optimally distributed and oriented during topology optimization of mechanical parts. Stiffness and weight are explicitly targeted in design, while other mechanical and biological functions are promoted implicitly through porosity and randomness of the spinodal features (e.g., increased buckling resistance, bone scaffolding for re-growth and repair). Microstructure images reproduced with permission: sand dollar[7] copyright 2010, Springer Nature; trabecular bone[8] copyright 2010, John Wiley and Sons; wood[2] copyright 2010, Cambridge University Press; horn[3] copyright 2010, Elsevier. All other images are original or free license.

(homogenization-based) topology optimization formulation proposed in 1988 by Bendsøe and Kikuchi,[14] which incepted the modern field of topology optimization, but has had limited success in practice due to manufacturing considerations (e.g., connectivity of locally oriented microarchitectures). Since then, several dehomogenization techniques have been pursued to map the oriented microarchitectures onto a smoothly-varying field,[15–17] or alternatively, several variations of multiscale topology optimization have been proposed that circumvent the need to orient the microarchitectures (e.g., concurrent approaches that simultaneously optimize the micro- and macroscale geometries[18,19]). Spinodal architected materials provide a means to obtain solutions with clear physical interpretation directly from Bendsøe and Kikuchi's original approach, without the need for laborious dehomogenization procedures; however, their integration with topology optimization has not been explored for design of 3D engineered parts with high levels of geometric complexity at multiple scales and manufacturing of such parts has yet to be demonstrated. These issues are addressed in the present work.

We pursue an extended version of Bendsøe and Kikuchi's original formulation that not only accommodates multiple candidate spinodal realizations, but also optimization of their locally-varying microscale orientation and density, as illustrated in **Figure 2**. In contrast to a recent data-driven approach that aims to span the entire space of spinodal architected materials for design of 2D structures,[20] we achieve a sufficiently rich design space by considering only one microarchitecture from each of the four anisotropic spinodal classes defined in Figure 1

and demonstrate the ability of spinodal embedding (in 3D) to outperform designs based on standard, density-based topology optimization (i.e., considering a single, solid, isotropic material). Each candidate spinodal architected material is characterized by a pre-defined restriction of the space of wave vectors defining the underlying GRF, but porosity and orientation are free to vary. The theoretical relevance of the approach is verified with a simple cantilever beam in which the selected spinodal microarchitectures align with the principal stress trajectories as predicted by Michell in 1904.[21] The practical relevance of the approach is demonstrated by designing and prototyping a stiff and lightweight jet-engine bracket and a porous craniofacial implant[22–24] that not only provides necessary mechanical function, but could also be used to promote bone regeneration with the use of biocompatible materials that stimulate cell growth.[7,25,26] Finally, making use of the functional representation of spinodal architected materials, the physical relevance of the approach is demonstrated by using a scalable, voxel-based method to translate the optimized, spinodal-encoded parts into manufacturable representations with seamless microscale-transitions and obtaining physical realizations using masked stereolithography (m-SLA) 3D printing.

2. Results and Discussion

Using a GRF to define the phase field of a spinodal architected material (see Equation (S2), Supporting Information)
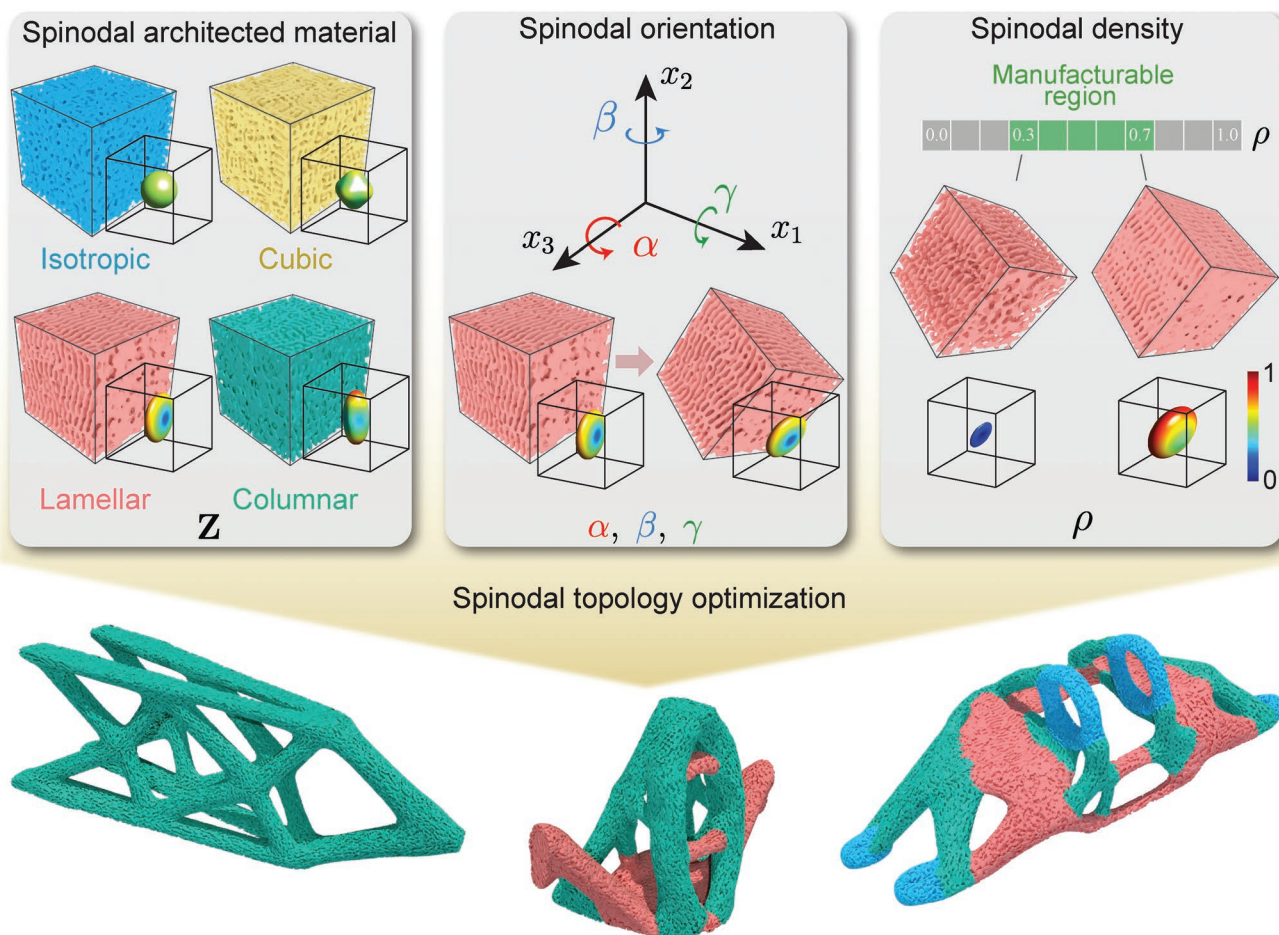
Figure 2. The spinodal topology optimization formulation pursued here consists of selecting a spinodal architected material from a subset of spinodal classes that cover a wide range of the anisotropic material space and choosing their porosity and orientation to promote stiffness and lightweightness.

provides a convenient avenue for: 1) tuning the anisotropy of various candidate spinodal architected materials; 2) aligning the variable-porosity microarchitectures along principal stress trajectories during topology optimization; 3) manufacturing spatially-varying microarchitectures without special treatment at transitions between different spinodal classes, orientations, or porosities; and 4) establishing a scalable, multiscale manufacturing framework in which macro and microscale features can be scaled independently and arbitrarily to satisfy requirements on separation of length scales, manufacturing constraints, or application-specific multiscale features.

The GRF is defined by a set of wave vectors defined on a unit sphere. By manipulating the stochastic distribution of the wave vectors, we can tune the resulting spinodal microarchitectures and associated constitutive behavior.[6] **Figure 3**a shows four particular distributions of the wave vectors (restricted according to cone angles, θ_1, θ_2, θ_3, as highlighted in colored patches on the unit sphere) that define one spinodal architected material from each of the four spinodal classes considered here (see Equation (S4), Supporting Information). Figure 3b illustrates how the mechanical properties of these spinodal architected materials vary with spinodal density, ρ, (i.e., the solid volume fraction of the spinodal microarchitecture) via components of

the associated stiffness elasticity tensor, $\mathbf{D}^H$, where the superscript, H, indicates that the mechanical properties are determined using computational homogenization[27] as discussed in Section S1.2, Supporting Information. As illustrated by the directional variation of their tensile modulus in Figure 3c, the isotropic class has equal stiffness in all directions, the cubic class has high stiffness along the three coordinate axes, the lamellar class has high stiffness in a single plane, and the columnar class has high stiffness along a single axis. Smaller cone angles increase directional bias of the spinodal architected materials and potentially allow for more efficient material use at the microscale, but also limit manufacturability (especially for the lamellar case) by reducing the connectivity of the spinodal microscale features. Nevertheless, with freedom to arbitrarily orient them and tune their porosity, these four choices of spinodal architected materials cover a wide range of the anisotropic microstructural-material space and facilitate spinodal topology optimization for increased optimality in multiscale, biomimetic structures.

The classical homogenization-based topology optimization formulation[14] is integrated with a recent multi-microstructural-material formulation[28] to simultaneously determine the macroscale geometry and the local existence, orientation, and
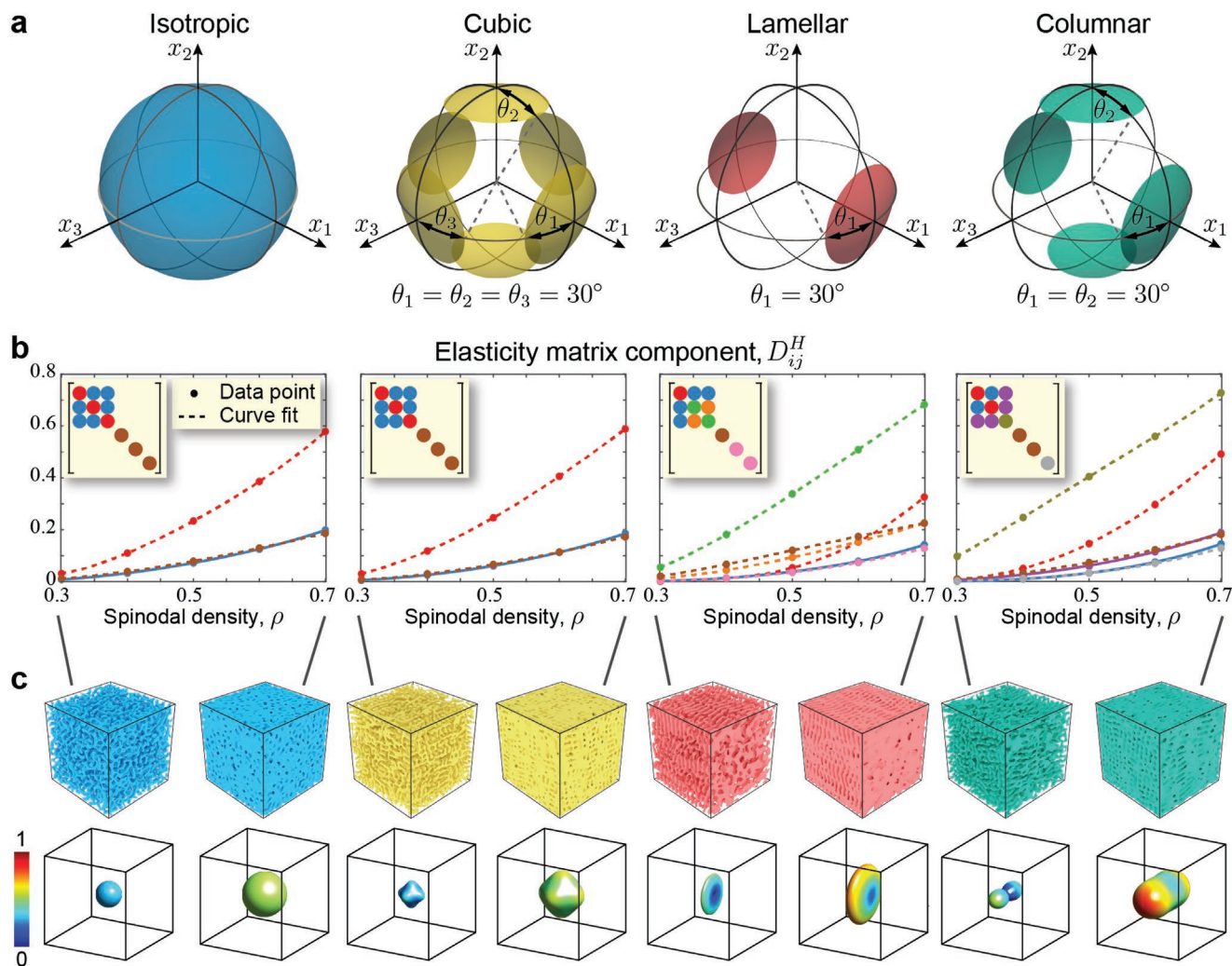
Figure 3. Definition of the isotropic, cubic, lamellar, and columnar candidate spinodal architected materials. a) Restricted space of wave vectors, n_i, defined by cone angles, θ_1, θ_2, θ_3. Regions indicated by color are those on the surface of the unit sphere where the wave vectors defining a given spinodal architected material can fall. b) Components of the homogenized stiffness elasticity matrix, D^H, as a function of spinodal density, ρ, in the manufacturable range. The data points for $\rho = 0.3, 0.4, 0.5, 0.6, 0.7$ are mean values obtained from the results of computational homogenization on fifteen realizations of each spinodal architected material. The curve fits are based on fourth-order polynomials. c) Idealized representation of each spinodal microarchitecture for $\rho = 0.3$ and $\rho = 0.7$ and associated elastic surfaces indicating the directional dependence of the tensile modulus.

porosity of m candidate spinodal architected materials in order to minimize the structural compliance, f, with limited material volume (here $m = 4$, for the four candidate spinodal architected materials defined in Figure 3). For this purpose, five sets of design variables are defined at N^e design points in the domain. The spinodal selection design variables, $\mathbf{Z} \in [0,1]^{N^e \times m}$, control the local presence or absence of each spinodal architected material; the spinodal density design variables, $\rho \in [\underline{\rho}, \overline{\rho}]^{N^e}$, control their local solid volume fraction; and the spinodal orientation design variables, $\alpha, \beta, \gamma \in [-\pi, \pi]^{N^e}$, control their local orientation. Note that the orientation design variables, which are used to locally orient the spinodal wave vectors associated with the underlying GRF, are defined using modular arithmetic with a period of 2π such that their domain is topologically equivalent to a circle and they can traverse directly from π to $-\pi$. Additional details of the spinodal topology optimization

formulation and solution scheme are provided in Section S2, Supporting Information.

Our homogenization-based approach enables us to perform topology optimization on a much coarser mesh than is required to define the spinodal features with sufficient detail and separation of scales. Note that the build volume of the m-SLA 3D printer used here can be thought of as a 3D matrix of pixels (pixel grid). During printing, each pixel is filled with material or no material based on a binary pixelated image projected to the underside of the resin vat for each layer of the part. Thus, the minimum length scale of the spinodal features is dictated by the resolution of the 3D printer's pixel grid, which can be much finer than the mesh used for topology optimization.

To decode the microscale features from the coarse topology optimization mesh, the design variables are projected to the fine pixel grid to obtain $\check{\mathbf{Z}} \in [0,1]^{N^p}$, $\tilde{\rho} \in [\underline{\rho}, \overline{\rho}]^{N^p}$,
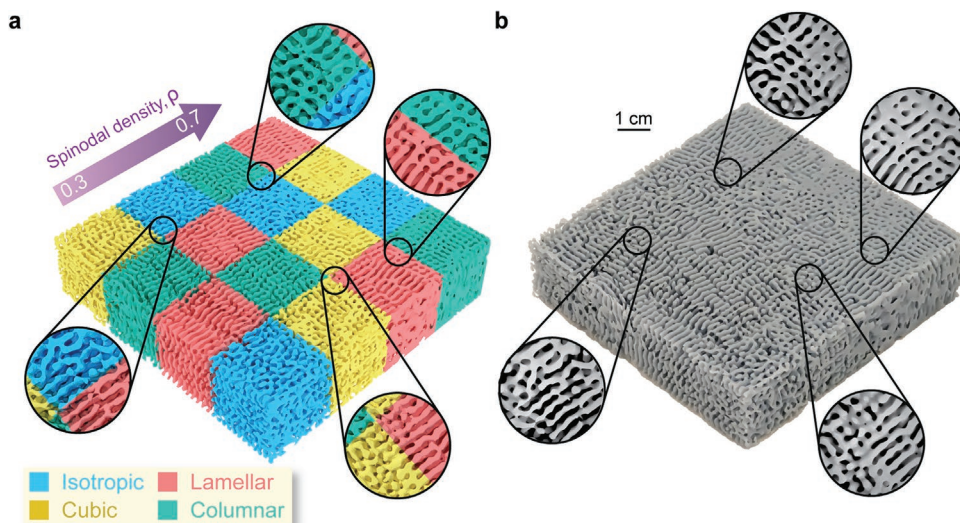
Figure 4. Tiling of the four spinodal architected materials illustrating seamless transitions between them. a) Numerical idealization and b) physical (manufactured) spinodal microstructures with undetectable transitions. The physical model in (b) has the exact geometrical features as those shown in the numerical idealization in (a).

and $\tilde{\alpha}, \tilde{\beta}, \tilde{\gamma} \in [-\pi, \pi]^{N^p}$, where N^p, is the number of pixels falling within the macroscale boundary defined in topology optimization by $\mathbf{Z}$. Then a discretized set of phase fields, $\phi_{\ell i}^0(\mathbf{x}_\ell, \tilde{\alpha}_\ell, \tilde{\beta}_\ell, \tilde{\gamma}_\ell), \ell = 1, \cdots, N^p, i = 1, \cdots, m$, that capture the locally-varying spinodal orientation (via orientation of the GRF's wave vectors) are computed for each spinodal architected material using Equation (S31), Supporting Information. The union of these phase fields does not guarantee well-connected spinodal features from one pixel to the next, but connectivity can be enforced by interpolating them according to the functional representation,

$$\phi_\ell(\mathbf{x}_\ell) = \frac{\sum_{i=1}^m \max\left[0, \left(1 - \frac{d_H(\mathbf{x}_\ell, \mathcal{M}_i)}{R_\phi}\right)\right]^{1/2} \phi_{\ell i}^0(\mathbf{x}_\ell, \tilde{\alpha}_\ell, \tilde{\beta}_\ell, \tilde{\gamma}_\ell)}{\sum_{i=1}^m \max\left[0, \left(1 - \frac{d_H(\mathbf{x}_\ell, \mathcal{M}_i)}{R_\phi}\right)\right]^{1/2}} \quad (1)$$

where $\mathcal{M}_i$ is the set of pixels in which spinodal architected material i dominates, d_H is the Hausdorff distance, and R_ϕ is the radius of the interpolated phase field that dictates the length scale of spinodal transitions, and $\ell = 1, ..., N^p$. The interpolation function in Equation (1) generates a smooth transition between the locally-varying spinodal architected materials, their orientations, and their densities (more detail is provided in Section S5.1 and Figure S5, Supporting Information). A discrete level set function,

$$\chi_\ell(\mathbf{x}_\ell) = \begin{cases} 1 & \text{if } \phi_\ell(\mathbf{x}_\ell) \geq \phi_{\text{cut}}(\tilde{\rho}_\ell) \\ 0 & \text{otherwise} \end{cases} \quad (2)$$

defines the final solid-void assignment of each pixel according to the spinodal density, $\tilde{\rho}$. Finally, 2D, binary, pixelated images corresponding to each layer of the spinodal-embedded topology-optimized part are obtained directly from the discrete level set field and sent to the 3D printer. A flowchart of the entire process from optimization-based

design to additive manufacturing is provided in Figure S6, Supporting Information.

As a demonstration, a spinodal tiling is generated in **Figure 4** from patches of phase fields associated with the four spinodal architected materials considered here. Only one of the four spinodal architected materials exists in each patch and the interpolation function in Equation (1) creates a single, connected field. The level set function in Equation (2) is defined from the interpolated phase field according to a linearly-varying spinodal density, $0.3 \leq \rho \leq 0.7$, as indicated in Figure 4a. The bounds on spinodal density, $\underline{\rho} = 0.3$ and $\overline{\rho} = 0.7$, ensure that the microstructure remains bicontinuous to avoid isolated solids at low spinodal densities and enclosed voids at high spinodal densities, which inhibit manufacturability.[13,29] A numerical and a physical (manufactured) representation of the spinodal tiling are shown in Figure 4a,b, respectively, where we observe that the transitions between the different spinodal architected materials are undetectable in the manufactured part. Note that the underlying GRF introduces randomness to the spinodal architected materials and Figure 4 only shows one specific realization.

2.1. Spinodal Architected Materials along Principal Stress Trajectories

The spinodal topology optimization formulation is first explored considering a cantilever beam for which we can readily make sense of the optimized solutions. Considering the design domain and boundary conditions defined in **Figure 5**a, the macroscale geometry of the cantilever beam is determined simultaneously with the spinodal class, orientation, and porosity at each point, with total material volume limited to $\overline{v} = 0.05$ of the domain volume (see Equation (S5), Supporting Information). The candidate spinodal architected materials are limited to those defined in Figure 3 with orientation free to vary

2109304 (5 of 10)
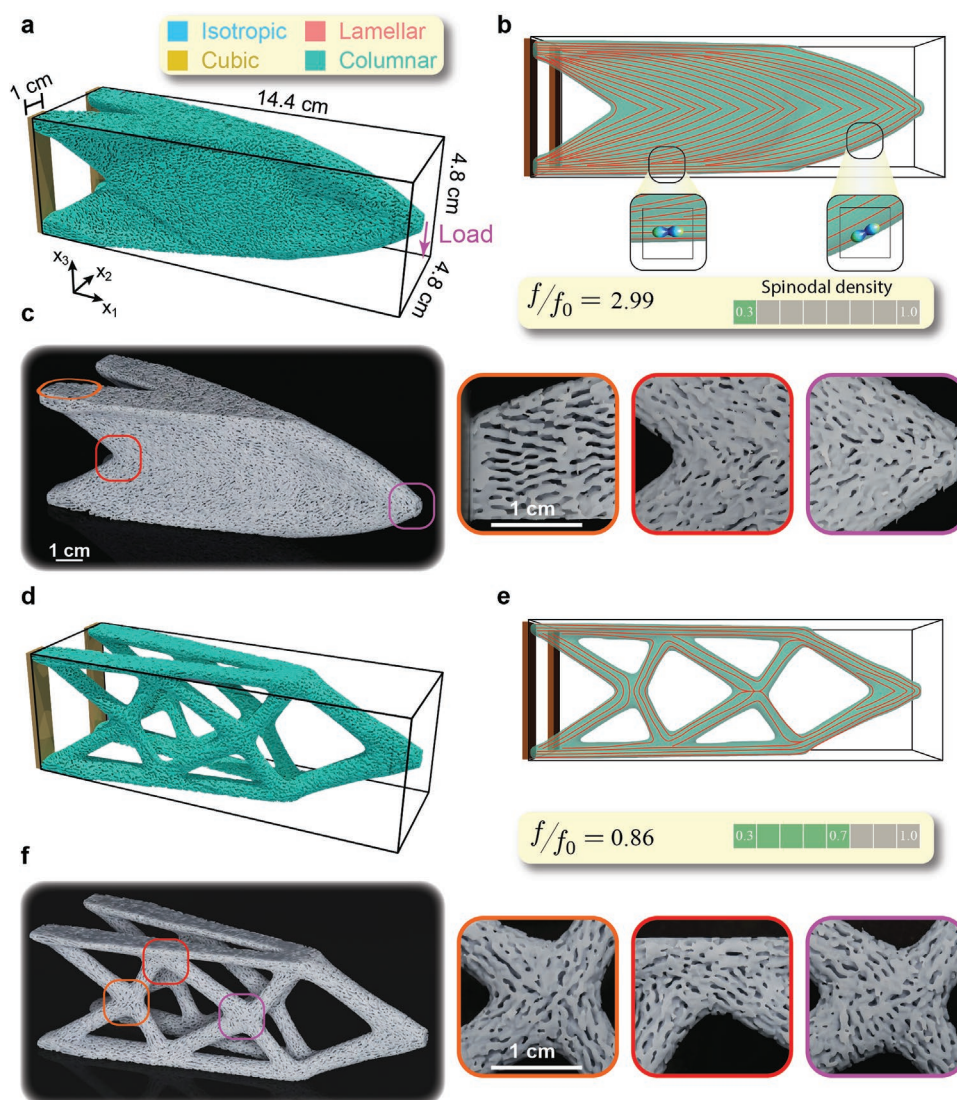
Figure 5. Optimized spinodal cantilever beams. a) Design domain, boundary conditions, and numerical solution for the cantilever beam with spinodal density limited to $\rho = 0.3$. Streamlines indicating the orientation of columnar spinodal microarchitecture's stiff axis and the manufactured part are provided in (b) and (c), respectively, for the $\rho = 0.3$ solution. d) Numerical solution for cantilever beam with spinodal density limited to $0.3 \leq \rho \leq 0.7$. Streamlines indicating the orientation of columnar spinodal microarchitecture's stiff axis and the manufactured part are provided in (e) and (f), respectively, for the $0.3 \leq \rho \leq 0.7$ solution. The objective function value of the standard (solid) solution is f_0 and $f/f_0 > 1$ indicates that the $\rho = 0.3$ spinodal solution is inferior to the standard (solid) solution and $f/f_0 < 1$ indicates that the $0.3 \leq \rho \leq 0.7$ spinodal solution outperforms the standard (solid) solution. Dimensions of the manufactured part agree with those indicated in (a).

arbitrarily in 3D space and spinodal density is limited to $\rho = 0.3$ in Figure 5a–c and $0.3 \leq \rho \leq 0.7$ in Figure 5d–f. The value, f/f_0, indicates the ratio of the compliance objective function values of the spinodal solution (f) to the standard topology optimization solution (f_0) considering a single, solid, isotropic material (the standard (solid) solution and associated f_0 is provided in Figure S3, Supporting Information).

When the spinodal density is limited to $\rho = 0.3$, high porosity enables the shell-like solution shown in Figure 5a. In contrast, when the spinodal density is free to vary in the manufacturable range, $0.3 \leq \rho \leq 0.7$, higher densities are preferred and the truss-like solution shown Figure 5d is needed to meet the macrostructural minimum length scale established by the density filter used in topology optimization (see Equation (S6), Sup-

porting Information). Within the restrictions of the topology optimization formulation considered here (e.g., macrostructure minimum length scale, prescribed spinodal microscale topologies, spinodal density bounds), the spinodal solutions approximate Michell's solutions in which material optimally aligns along principal stress trajectories.[21] Note that both spinodal solutions select only the columnar spinodal microarchitecture and align its stiff axis along the principal stress trajectories of the macrostructure as indicated by the streamlines in Figure 5b,e, which are instantaneously tangent to the locally oriented x_3 axis of the columnar elastic surface (refer to the coordinate frame in Figure 3). By aligning the columnar axis of high stiffness with the principal stress trajectories, a shear-free stress state is obtained in regions of the beam where shear is

typically expected. In the truss-like solution, the stiff axis of the columnar spinodal architected material is locally oriented along the axes of the truss members to efficiently take the expected tension and compression.

With more freedom in spinodal density, the truss-like solution outperforms the standard solid solution as indicated by $f/f_0 < 1$. This result highlights a benefit of spatially-varying spinodal architected materials over widely-used lattice microarchitectures. Due to limited tunability of anisotropic properties and difficulty in guaranteeing connectivity for oriented lattices, lattice-embedded parts tend to have degraded mechanical performance relative to the standard solid solution.[28] As shown in Figure S4a, Supporting Information, over 60% of the solution with $f/f_0 < 1$ contains spinodal density in the range $0.65 \leq \rho \leq 0.7$ and just under 20% contains spinodal density in the range $0.3 \leq \rho \leq 0.35$. In pursuit of high porosity, the objective function value of the shell-like solution is sacrificed and performance is worse than that of the standard (solid) solution (i.e., $f/f_0 > 1$). Nevertheless, higher porosity may be of interest to satisfy design requirements not explicitly integrated into the topology optimization statement (e.g., biological function,

buckling resistance). It is also noted that, although not enforced explicitly in design, the spinodal-embedded truss members may be more adept at resisting load and geometry uncertainties as a result of the stochastic nature of spinodal microarchitectures. The manufactured shell-like and truss-like solutions are provided in Figure 5c,f, respectively. Each manufactured beam has length 14.4 cm and close-up views of the embedded spinodal microarchitectures illustrate agreement between the streamlines and local material alignment.

2.2. Optimal Design and Spinodal Embedding of GE Jet Engine Bracket

The spinodal architected materials defined in Figure 3 are also considered in the design of a jet engine bracket from General Electric (GE) in pursuit of a lightweight part.[30] The design domain and boundary conditions are provided in **Figure 6**a. Here, two load cases are considered and the objective function, f, is taken as the sum of compliance associated with each load case. Spinodal density is allowed to vary in the full manufacturable
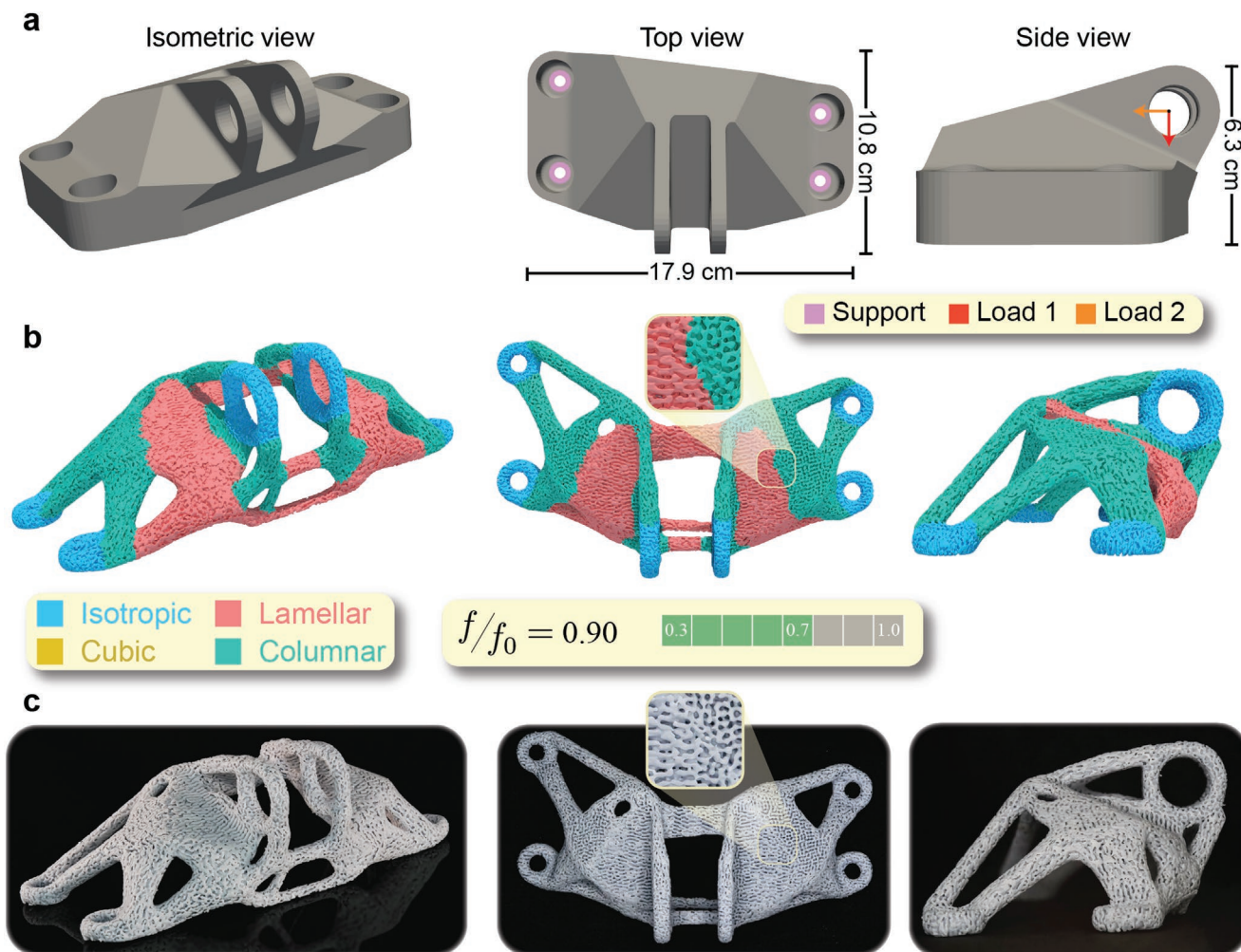
Figure 6. Optimized spinodal GE jet engine bracket. a) Design domain and boundary conditions. b) Numerical solution with idealized spinodal architected materials embedded. c) Spinodal-embedded manufactured part. The value $f/f_0 < 1$ indicates that the spinodal solution outperforms the standard solid solution. Dimensions of the manufactured part agree with those indicated in (a).

**ADVANCED
SCIENCE NEWS**
www.advancedsciencenews.com

**ADVANCED
MATERIALS**
www.advmat.de

range, $0.3 \leq \rho \leq 0.7$, and the total material volume of the structure is limited to $\overline{v} = 0.075$ of the domain volume.

The much more complex design domain and loading conditions considered here lead to selection of more than one spinodal architected material during optimization (see Figure 6b). Again, the columnar spinodal microarchitecture tends to locally align its stiff axis along the truss-like legs of the structure, but the lamellar and isotropic spinodal microarchitectures are also used in regions that may be subjected to loading in multiple directions. The constitutive behavior of the isotropic and cubic spinodal architected materials in Figure 3b explains why the cubic spinodal architected material is not used anywhere in the part. The cubic spinodal architected material has slightly higher stiffness than the isotropic in directions aligned with the coordinate axes, but is less stiff in all other directions. Thus, if multiple, non-orthogonal components of loading are present at a design point, isotropic will be preferred over cubic. The variation of spinodal density for the GE bracket design is provided in Figure S4, Supporting Information. Spinodal densities near the bounds are preferred, but slightly more intermediate values are used in comparison to the cantilever problem. Again, the freedom in spinodal density leads the spinodal solution to outperform the standard (solid) solution as indicated by $f/f_0 < 1$ (the standard (solid) solution, considering a single, solid, isotropic material, and the associated f_0 are provided in Figure S3, Supporting Information).

The manufactured GE bracket shown in Figure 6c has dimensions consistent with those indicated in Figure 6a. The insets in Figure 6b,c show the well-connected interface between the lamellar and columnar spinodal microarchitectures and the agreement between the expected and manufactured spinodal features. Due to dimensional limitations of the 3D printer, the spinodal-embedded GE bracket was printed in two parts and assembled. Decomposition of the part was facilitated by the functional representation of the spinodal features. A standard additive manufacturing procedure would require cutting a spinodal-embedded surface representation (STL). Not only would the spinodal-embedded STL with the desired microscale resolution be excessively memory intensive, ensuring that the decomposed STLs are watertight and that they fit together for assembly is nontrivial. On the other hand, the proposed approach enables us to simply increase the number of pixels in the pixel grid, decode the spinodal features onto it, and then divide the pixel grid into subsets that coincide with our 3D printer's capabilities.

2.3. Optimal Design and Spinodal Embedding of Porous Craniofacial Implant

Topology optimization has been used to design patient-specific craniofacial implants for those suffering from traumatic facial injuries.[22,23] Previous work in topology optimization focused on obtaining the shape needed to fill the space and support mechanical loads (e.g., masticatory forces), but did not attempt to provide the porosity needed to promote bone regeneration. On the other hand, spinodal microarchitectures have been found more capable of promoting bone re-growth than other architected materials.[26] Here, a craniofacial implant is

designed using spinodal topology optimization considering the four spinodal architected materials shown in Figure 3 such that both mechanical demands and porosity are targeted in design. The design domain shown in **Figure 7**a was provided by Dr. Tomás Zegard and corresponds to the dimensions of his own face.[24] The total material volume is limited to $\overline{v} = 0.05$ of the domain volume.

Several researchers have found that bone formation is promoted when the scaffold porosity and pore size are 50–90% and 100–400 µm, respectively.[31,32] Porosity can be controlled directly in the topology optimization formulation by setting the spinodal density bounds. Pore size can be controlled during manufacturing by selecting the wavelength parameter of the GRF, κ (see Equations (S2) and (S31) and Figure S1, Supporting Information). In Figure 7b, solutions considering two different sets of spinodal density bounds are compared. The numerical solutions and additional details of the manufactured parts are provided in Figure 7c,d. The solution in Figure 7c aims for the highest achievable porosity of around 70% by setting the spinodal density to the smallest value that ensures a well connected microarchitecture ($\rho = 0.3$). This solution has the desired porosity, but performs worse than the standard (solid) solution as indicated by $f/f_0 > 1$ (see standard (solid) solution in Figure S3, Supporting Information). The solution in Figure 7d with spinodal density, $0.3 \leq \rho \leq 0.7$, leads to a design with better mechanical performance ($f/f_0 < 1$), but the average porosity is 40%, which is outside of the desired range (see spinodal density variation in Figure S4, Supporting Information). Both solutions make use of only the columnar and lamellar spinodal microarchitectures, and although they contain the same volume of the bulk material, the increased porosity in the $\rho = 0.3$ solution leads to a bulkier design than that of the $0.3 \leq \rho \leq 0.7$ solution. The desired scaffold pore size (100–400 µm) is close to the achievable resolution of the 3D printer. For demonstration purposes, the pores are printed at more than twice the desired size by choosing $\kappa = 4$ cm^{-1}, but this value can be tuned depending on the manufacturing platform and the specific application.

Although only designed for stiffness and weight, the spinodal-embedded craniofacial implants could be explored with biocompatible materials for use as prosthetics or bone scaffolds that also promote regeneration and repair. The ability to carefully control porosity and pore size by tuning parameters of the spinodal phase field and/or the optimization problem, serves to expand the application space and enhance customization capabilities.

3. Conclusion

We unified optimal design and manufacturing of spinodal-embedded multiscale structures by integrating spinodal architected materials with tunable anisotropy into a spinodal topology optimization framework. In this way, we simultaneously find an optimized macroscale geometry and the distribution of different spinodal architected materials at the microscale, with freely-varying orientation and porosity. In the resulting designs, microscale features tend to align with principal stress directions for efficient material use in supporting mechanical demands. In addition to improving the target
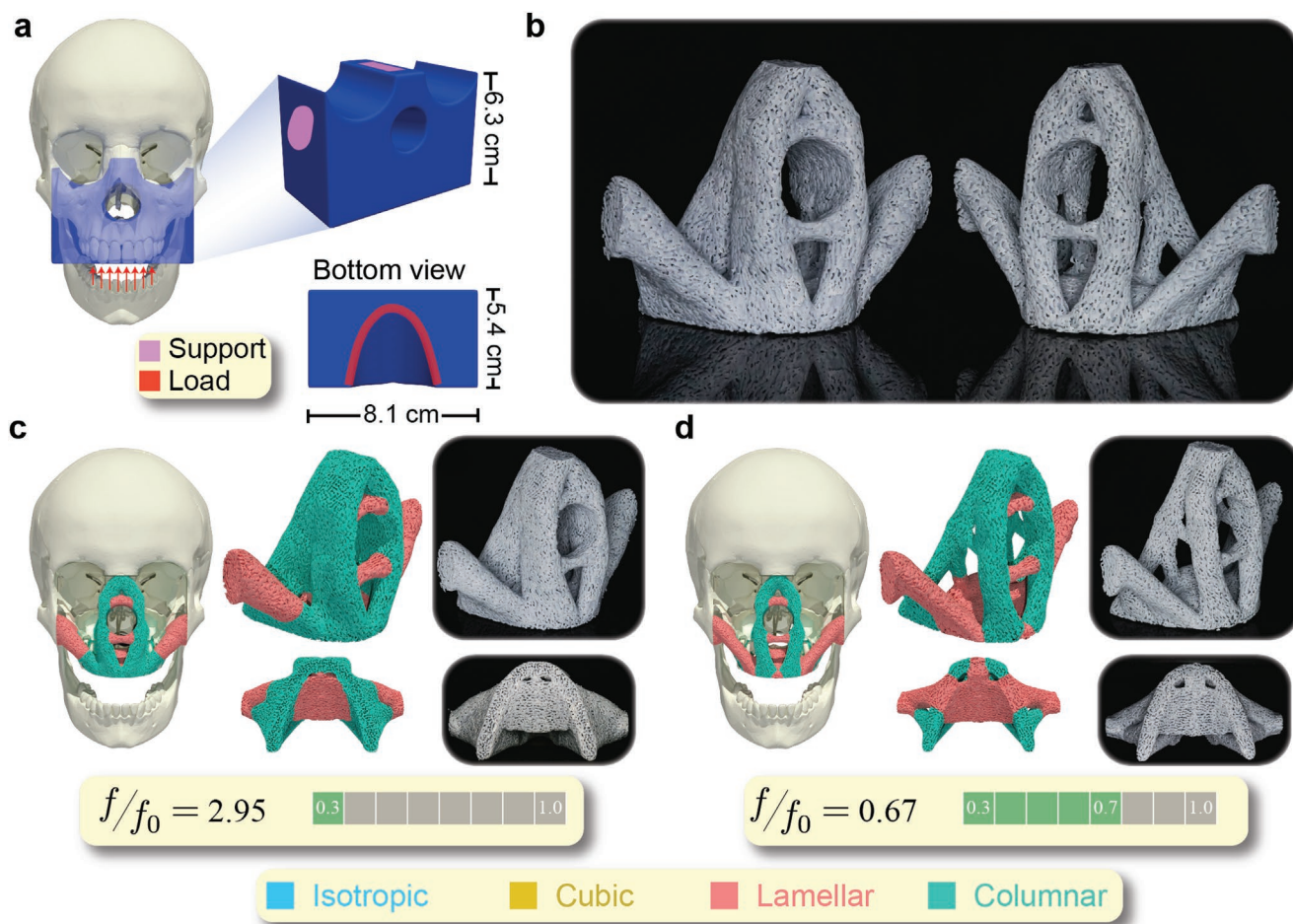
Figure 7. Optimized spinodal craniofacial implants. a) Design domain and boundary conditions. b) Comparison of solutions with spinodal density limited to $\rho = 0.3$ and $0.3 \leq \rho \leq 0.7$ on the left and right, respectively. The numerical solution with idealized spinodal architected materials embedded and spinodal-embedded manufactured part are provided in (c) and (d) for the $\rho = 0.3$ and $0.3 \leq \rho \leq 0.7$ solutions, respectively. Dimensions of the manufactured parts agree with those indicated in (a), which are based on measurements of Dr. Tomás Zegard's face.[24]

mechanical performance, the porosity and randomness of the spinodal architected materials also indirectly endow the structures with various other mechanical and biological functions (e.g., tunable pores that can promote bone regeneration and re-growth). At the same time, the functional representation of spinodal microarchitectures leads to a clear physical interpretation that can be manufactured directly, without special treatment at spinodal transitions and that provides significant freedom to independently tune the macro and micro length scales for application-specific or other practical considerations.

Looking forward, we anticipate that spinodal topology optimization and additive manufacturing may have even greater impact in problems like energy absorption, thermal control, fluid flow, acoustic filtering, and wave scattering than in the stiffness maximization problem pursued here, which will require integration with other physics and more sophisticated homogenization techniques. Even within the scope of elastostatics, it is necessary to investigate the effect of the transitions between the spinodal classes, orientations, and porosities; the appropriate separation of length scales; and whether the spinodal material properties (insensitivity to imperfections and high energy absorption[10,11]) transfer to the macroscale structure.

Supporting Information

Supporting Information is available from the Wiley Online Library or from the author.

Conflict of Interest

The authors declare no conflict of interest.

ADVANCED
SCIENCE NEWS

www.advancedsciencenews.com

ADVANCED
MATERIALS

www.advmat.de

Data Availability Statement

The data that support the findings of this study are available from the corresponding author upon reasonable request.

[1] P. Fratzl, R. Weinkamer, *Prog. Mater. Sci.* **2007**, *52*, 1263.
[2] L. J. Gibson, M. F. Ashby, B. A. Harley, *Cellular Materials in Nature and Medicine*, Cambridge University Press, **2010**, *9*, 83.
[3] L. Tombolato, E. E. Novitskaya, P.-Y. Chen, F. A. Sheppard, J. McKittrick, *Acta Biomater.* **2010**, *6*, 319.
[4] H. M. Frost, *Anat. Rec.* **1987**, *219*, 1.
[5] H. M. Frost, *Anat. Rec., Part A* **2003**, *275*, 1081.
[6] S. Kumar, S. Tan, L. Zheng, D. M. Kochmann, *npj Comput. Mater.* **2020**, *6*, 73.
[7] A. Barreiro, D. Recouvreux, D. Hotza, L. Porto, C. Rambo, *J. Mater. Sci.* **2010**, *45*, 5252.
[8] X. S. Liu, X. H. Zhang, C. S. Rajapakse, M. J. Wald, J. Magland, K. K. Sekhon, M. F. Adam, P. Sajda, F. W. Wehrli, X. E. Guo, *J. Bone Miner. Res.* **2010**, *25*, 2039.
[9] C. M. Portela, A. Vidyasagar, S. Krödel, T. Weissenbach, D. W. Yee, J. R. Greer, D. M. Kochmann, *Proc. Natl. Acad. Sci. U. S. A.* **2020**, *117*, 5686.
[10] A. Guell Izard, J. Bauer, C. Crook, V. Turlo, L. Valdevit, *Small* **2019**, *15*, 1903834.
[11] M.-T. Hsieh, B. Endo, Y. Zhang, J. Bauer, L. Valdevit, *J. Mech. Phys. Solids* **2019**, *125*, 401.
[12] J. W. Cahn, *J. Chem. Phys.* **1965**, *42*, 93.
[13] C. Soyarslan, S. Bargmann, M. Pradas, J. Weissmüller, *Acta Mater.* **2018**, *149*, 326.
[14] M. P. Bendsøe, N. Kikuchi, *Comput. Methods Appl. Mech. Eng.* **1988**, *71*, 197.
[15] O. Pantz, K. Trabelsi, *SIAM J. Control Optim.* **2008**, *47*, 1380.
[16] G. Allaire, P. Geoffroy-Donders, O. Pantz, *Comput. Math. Appl.* **2019**, *78*, 2197.
[17] J. P. Groen, O. Sigmund, *Int. J. Numer. Methods Eng.* **2018**, *113*, 1148.
[18] H. Rodrigues, J. M. Guedes, M. Bendsoe, *Struct. Multidiscip. Optim.* **2002**, *24*, 1.
[19] L. Liu, J. Yan, G. Cheng, *Comput. Struct.* **2008**, *86*, 1417.
[20] L. Zheng, S. Kumar, D. M. Kochmann, *Comput. Methods Appl. Mech. Eng.* **2021**, *383*, 113894.
[21] A. G. M. Michell, *London, Edinburgh Dublin Philos. Mag. J. Sci.* **1904**, *8*, 589.
[22] A. Sutradhar, G. H. Paulino, M. J. Miller, T. H. Nguyen, *Proc. Natl. Acad. Sci. U. S. A.* **2010**, *107*, 13222.
[23] A. Sutradhar, J. Park, D. Carrau, T. H. Nguyen, M. J. Miller, G. H. Paulino, *Med. Biol. Eng. Comput.* **2016**, *54*, 1123.
[24] T. Zegard, G. H. Paulino, *Struct. Multidiscip. Optim.* **2016**, *53*, 175.
[25] V. Karageorgiou, D. Kaplan, *Biomaterials* **2005**, *26*, 5474.
[26] M.-T. Hsieh, M. R. Begley, L. Valdevit, *Mater. Des.* **2021**, *207*, 109838.
[27] A. Bensoussan, J.-L. Lions, G. Papanicolau, *Asymptotic Analysis for Periodic Structures*, Elsevier, New York **1978**.
[28] E. D. Sanders, A. Pereira, G. H. Paulino, *Sci. Adv.* **2021**, *7*, eabf4838.
[29] A. Vidyasagar, S. Krödel, D. M. Kochmann, *Proc. R. Soc. A* **2018**, *474*, 20180535.
[30] G. Electric, GE jet engine bracket challenge, https://grabcad.com/challenges/ge-jet-engine-bracket-challenge (accessed: March 2021).
[31] M. Vranceanu, I. Antoniac, F. Miculescu, R. Saban, *J. Optoelectron. Adv. Mater.* **2012**, *14*, 671.
[32] L. Zhu, D. Luo, Y. Liu, *Int. J. Oral Sci.* **2020**, *12*, 6.